ACS OMEGA

http://pubs.acs.org/journal/acsodf

Article

KNO_3-Loaded Coffee Husk Ash as a Heterogeneous Alkali Catalyst for Waste Frying Oil Valorization into Biodiesel

Demelash Tilahun Bekele, Nurelegne Tefera Shibeshi,* and Ali Shemsedin Reshad

Cite This: *ACS Omega* 2022, 7, 45129−45143

Read Online

ACCESS | Metrics & More | Article Recommendations

ABSTRACT: In this study, a heterogeneous basic catalyst was synthesized from a catalyst composite material (CCM) of coffee husk ash and char mixture (A/C) impregnated with KNO_3 and employed to transesterify crude waste frying oil (WFO). The effect of CCM calcination temperature (CCMCT) (500−700 °C) on the catalyst physicochemical properties was investigated. A differential scanning calorimeter was used to examine potential phase changes during the calcination of A/C and CCM. The catalysts from each CCMCT were characterized by X-ray diffraction (XRD), Brunauer−Emmet−Teller surface area analyzer, scanning electron microscopy (SEM), SEM with energy-dispersive X-ray diffractometer, colorimeter, and attenuated total reflectance Fourier transform infrared (ATR-FTIR) spectrometer. The methoxy functional group FTIR peak integral value and the dynamic viscosity of the biodiesel synthesized by each catalyst were used to determine the qualitative WFO conversion. Furthermore, the quantitative WFO conversion was determined using nuclear magnetic resonance (^{1}H NMR) analysis. Crystallinity, elemental composition, basicity, and morphology of catalysts were highly dependent on the CCMCT. Without transesterification condition optimization (reaction temperature of 45 ± 2.5 °C, catalyst loading of 3 wt %, methanol to oil molar ratio of 12:1, and reaction time of 1 h), a higher catalytic performance (72.04% WFO conversion) was reached using a catalyst from the CCMCT of 600 °C. When using a coffee husk ash catalyst without KNO_3 impregnation (C-00-600), the WFO conversion was only 52.92%. When comparing the C-25-600 and C-00-600 catalysts, it was observed that KNO_3 impregnation had a substantial impact on the catalyst crystallinity, basicity, and morphology.

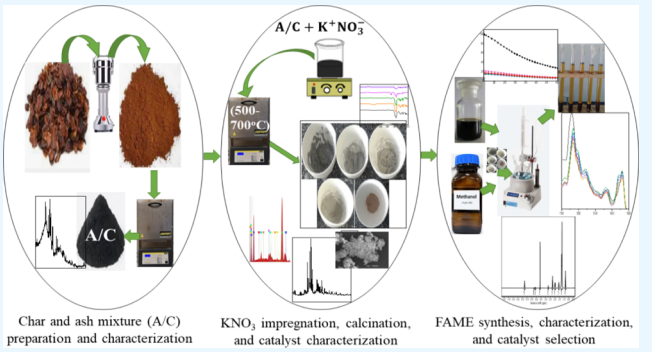

INTRODUCTION

From an economic and environmental pollution perspective, relying on fossil fuels as a primary source of energy is unreliable in the future generation.[1] That is why the world's attention is shifting toward biofuels.[2] Among biofuels, biodiesel is the best alternative to replace fossil diesel fuel. The benefits of biodiesel include lower overall exhaust emission gases and toxicity, biodegradability, sourcing from renewable and domestic feedstocks, low sulfur content, superior flashpoint, improved combustion efficiency, and a 78% reduction in net CO_2 emissions based on life cycle assessment.[3−5]

Unless non-edible and low-grade fat and oils are employed in the transesterification reaction, large-scale biodiesel production cannot be feasible.[6] Therefore, engaging waste frying oils (WFOs) to produce biodiesel is economical, minimizes the competition between food and fuel, and reduces pollution from WFO residue.[2,7] However, the transesterification of low-grade feedstocks such as WFO is ineffective without a suitable catalyst. Homogeneous, heterogeneous, and enzyme catalysts were investigated. Alkali homogeneous catalysts are being used in most existing biodiesel plants. However, soap formation, which makes product separation challenging, rendered their utilization unsuitable for feedstocks containing significant FFA (>1%).[8] Even though acidic catalysts hinder soap formation via simultaneous esterification and transesterification, they are corrosive to reactors and do not provide sufficient catalysis.[9] The enzyme catalysts are nonpolluting and with high selectivity. They have downsides including a longer reaction time, high cost, and deactivation in the presence of methanol.[10,11] Nowadays most investigations are converging toward heterogeneous solid catalysts because of their reusability and renewability.[12,13] Similarly, the use of heterogeneous catalysts can also increase the sustainability of biodiesel production for future generations and reduce the production cost of biodiesel.[2,12] Furthermore, while using

Received: August 29, 2022
Accepted: November 15, 2022
Published: November 30, 2022

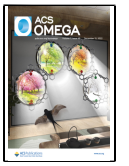

https://doi.org/10.1021/acsomega.2c05572
ACS Omega 2022, 7, 45129−45143

heterogeneous catalysts, greater purity glycerin can be obtained with fewer dissolved ions.[14]

The main barrier to the use of heterogeneous catalysts is their high cost. Exploration of a cheap precursor that gives a high-performing catalyst is necessary to overcome the economic constraints in the next generation for the mass production of biodiesel.[15] Because of catalyst typical traits, including thermal and mechanical stability and low cost, metal oxides are frequently employed in the synthesis of heterogeneous catalysts.[16] The catalytic activity depends on the base or acid strength and active site concentration.[17] The catalyst texture and degree of crystallinity also matter.[18] These catalyst properties depend on the catalyst synthesis condition and precursor composition. Although it was not always the case, most metallic oxides showed better stability and catalytic activity when mixed with other oxides or integrated with porous supports.[19−24]

Mixed oxide catalysts can be synthesized from chemical and biological sources. In this field, heterogeneous catalysts made from agricultural wastes with little economic value have emerged, and they are projected to lower the cost of biodiesel synthesis.[25] Lignocellulosic biomass (LB), one of the several precursors for mixed oxides, is eco-friendly and renewable. The synthesis of heterogeneous catalysts can use LB-derived ash directly as a catalyst or active site support.[26,27] Ash from LB can be used as an alkali heterogeneous catalyst or precursor if it is rich in alkali metal (particularly K, Ca, and Mg) compounds.[28,29] Based on catalyst synthesis conditions (mainly calcination), these compounds can be transformed into a variety of forms, including metal oxides. During basic catalyst synthesis, the basicity (basic strength) of a catalyst is very important parameter.[26] K_2O is more strongly basic than CaO and MgO. KNO_3 is a possible source of K_2O which increases the basicity of the catalyst.[30,31] The K and Ca compounds have a synergetic impact on transesterification and higher K content in ashes ensures stronger basicity.[25] For instance, Babajide et al. 2010[32] prepared a basic catalyst by KNO_3 (which later decomposed into K_2O during calcination) impregnation to silica-rich ash. Similar phenomena were also observed from KNO_3-loaded zeolite.[33] Also, the decomposition of K_2CO_3 and $CaCO_3$ in the LB ash may be facilitated due to a chemical modification.[34]

In addition to the calcination condition, the composition of LB-derived ash depends strongly on the LB type.[26] Various LBs were investigated for alkali catalyst synthesis. Waste *Musa paradisiaca*,[29] *Mangifera indica* peel,[28] pineapple leaves,[35] and waste *Sesamum indicum* plant[36] are a few examples. In this study, coffee husk (CH) ash was proposed as a basic catalyst precursor based on its reported chemical composition [K_2O (46.46%) and CaO (17.7%)].[37] KNO_3 was also incorporated into the CH ash to make the catalyst composite material (CCM). The influence of CCM calcination temperature on the physicochemical properties and performance of CH-derived catalyst was studied in particular. To the best of our knowledge, the catalytic activity of CH ash and its derivative has been rarely investigated.

MATERIALS AND METHODS

Materials. WFO was obtained from local pan-fried fish sellers and coffee (Yirga Cheffe) husk was collected from local agro-processing units around Dilla, Ethiopia. Chemicals such as potassium nitrate (98%), phenolphthalein indicator (≥99%), methanol (≥98%), toluene (99.8%), benzoic acid (≥99.5%), potassium hydroxide (85%), sodium hydroxide (97%), and ethanol (≥98%) were purchased from local retailers in Addis Ababa Ethiopia.

Methods. *WFO Pretreatment and Characterization.* The crude WFO was heated and filtered to remove solid impurities and contaminants. The filtered WFO was further heated to 90 °C for 1 h to remove moisture.[38] Then, it was poured into a clean container and maintained sealed for further use. The treated WFO acid and saponification values were determined using ISO 660:2020 and AOCS 920.160 standard procedures, respectively.

CH Preparation and Characterization. A dried fine CH powder was prepared by washing the raw CH with tap water, sun drying for 15 days, oven drying at 105 °C for 3 h, and grinding with a coffee grinder (NIMA NM-124, China). A fine CH powder (≤250 μm) was employed during CH characterization. The CH moisture content was determined by the test approach given in the ASTM standard E1756-08. The ASTM standards E1755-01 and E872-82 were used to determine the ash and volatile matter content of the CH, respectively.

Catalyst Synthesis. The CCM was prepared by a capillary impregnation of KNO_3 onto ash and char mixture (A/C). The A/C was prepared by calcination of CH powder (60 g in a dished crucible) in a muffle furnace (Nabertherm P330, Germany) at 600 °C for 2 h. Adding excess distilled water during KNO_3 impregnation may cause the leaching of K_2CO_3.[39] Therefore, titration of the A/C with distilled water was first performed to determine the A/C pore volume. Then, the impregnation was done by mixing the KNO_3 with 12 mL of distilled hot water (35 °C) for 5 min, followed by 12 g of A/C addition into the solution. In comparison to the ash content of A/C, the KNO_3 weight percentage was kept at 25%. After impregnation, the CCM was dried in a static air oven at 105 °C for 4 h. Finally, the CCM was thermally activated with a heating rate of 10 °C/min in the muffle furnace. During the calcination process, the furnace vent system was opened for calcination products and air exchange.

To determine the effect of calcination temperature on the catalyst physicochemical properties, CCM was calcined for 3 h (at 500, 550, 600, and 650 °C) and 2 h (at 700 °C). The catalysts were designated as C-25-500, C-25-550, C-25-600, C-25-650, and C-25-700. For comparison purposes, catalysts were also prepared by calcination of the ash and char mixture (A/C) at 600 and 700 °C for 3 and 2 h, respectively, without KNO_3 impregnation. These catalysts were designated by C-00-600 and C-00-700, respectively. The first and second numbers after the letter C in the catalyst designation stand for KNO_3 weight percentage and CCM calcination temperatures, respectively.

Solid Materials and Product Characterization. For the A/C and CCM, DSC (SKZ1052B, China) analysis under a nitrogen (120 mL/min) environment was done. The temperature range was 25−700 °C at a heating rate of 10 °C/min. A spectrophotometer (CM-600d, Japan) was employed to measure the color of the catalysts. Before performing a color test of each catalyst sample, the spectrophotometer was subjected to zero calibration followed by white calibration. Following calibrations, the average values of three measurements of each sample's CIE-$L^*a^*b^*$ color space values were recorded. The crystalline phases of the A/C, CCM, and catalysts were distinguished by an X-ray diffractometer (Shimadzu XRD-7000, Japan), with Cu Kα radiation (λ = 0.15406 nm) and operating at 40 kV and 30 mA. The 2θ values

https://doi.org/10.1021/acsomega.2c05572
ACS Omega 2022, 7, 45129−45143

range from 10 to 80° with a step size of 0.02° and a scanning speed of 3°/min. To find out which crystalline phases were present, peak 2θ values were contrasted with 2θ values found in the literature. The surface area of catalysts was determined by the surface area analyzer (Horiba Instruments, Inc. SA-9600 series, USA) using the Brunauer−Emmet−Teller (BET) method. Before the surface area analysis, each catalyst was heated overnight at 110 °C in an oven after proper size reduction with mortar and pestle. Furthermore, the catalyst samples were degassed by the surface area analyzer degassing process step at 150 °C for 3 h. Nitrogen was adsorbed by the catalyst in a liquid form by keeping the bath at 77 K. The linear BET curve was generated by measuring the number of N_2 molecules adsorbed at three relative pressures (0.1, 0.2, and 0.3).

The catalysts surface morphology was characterized by a scanning electron microscope (JCM-6000Plus, German). The accelerating voltage was 15 kV. A scanning electron microscope with energy-dispersive X-ray (SEM−EDX) analysis was employed to determine the elemental composition of catalysts. When analyzing catalyst and intermediate products for the identification of functional groups, a Fourier transform infrared spectrometer (Thermo Scientific Nicolet, IiS50 ABX smart iTX) with an attenuated total reflectance ATR (diamond crystal) and DTGS KBr detector was utilized. The scanning range was from 400 to 4000 cm^{-1} with a resolution of 2 cm^{-1} and 32 numbers of scanning.

Catalysts Basicity Measurement. To assess the total basicity of the catalysts, the Hammett indicator (phenolphthalein) and 0.1 N benzoic acid in toluene as a titer were utilized.[40] For the first 30 min, a suspension of 0.15 g of catalyst in phenolphthalein solution in toluene (2 mL, 0.1 mg/mL) was agitated. Finally, the benzoic acid solution in toluene (0.01 M) was used to titrate the suspension. The titration endpoint was identified by the mixture's transformation from pink to colorless.

The leachable basicity determination was started by shaking 0.5 g of catalyst in 50 mL of distilled water for 1 h at room temperature. Then, the solution was filtered to get a clean filtrate free of catalyst particles. The clear filtrate was mixed with a methanol solution of phenolphthalein (5 mL, 0.1 mg/L) and titrated using a toluene solution of benzoic acid (0.01 M).[40]

Transesterification Reaction and Post-Treatment Process. For each catalyst, an activity test was conducted by the transesterification of the crude WFO using a reaction condition stated by Vyas et al. 2009,[41] Ayoola et al. 2020,[30] and a preliminary study. A reflux setup comprising a 500 mL three-necked round-bottomed flask reactor and a tap water-cooled condenser was used to carry out the transesterification procedures. A 3 wt % catalyst was first stirred in the reactor with methanol for 30 min at 400 rpm by keeping the reaction temperature at 45 ± 2.5 °C. Once the 30 min methoxide formation time is elapsed, WFO (16.67 g) which was heated to the reaction temperature was added to the reaction mixture and the rpm increased to 600. The transesterification reaction duration was 1 h with an alcohol-to-oil molar ratio of 12:1.[31] After completion of the stipulated reaction time followed by cooling, the reaction mixture was centrifuged at 1200 rpm for 15 min. The separated phase was aged overnight for further separation of glycerol. The upper layer was extracted by a pipette and washed with hot water (at 55 °C, 2:1 distilled water to biodiesel volume ratio, 20 min, and 4 cycles) to remove the remaining impurities. Then, the biodiesel was dried at 110 °C for 24 h in a static air oven to remove the remaining water.[42] Purified and dried biodiesel was labeled BID-x depending on the catalyst (C-25-x) type employed, where x belongs to the CCMCT in the range of 500 to 700 °C. The biodiesel synthesized using the C-00-600 catalyst was designated by BID-00-600. The purified biodiesel was then stored in an airtight container for subsequent analysis.

Qualitative and Quantitative Analysis of WFO Conversion. The FTIR spectra regions 1188−1200 cm^{-1} (because of −O−CH_3 stretching) and 1425−1447 cm^{-1} (because of CH_3 asymmetric bending) were nominated for qualitative analysis of biodiesel yield.[43,44] In these regions, biodiesel had a peak but not the WFO. The dynamic viscosity of biodiesel in mPa s at 40 °C measured using a Rheometer (MCR 102 SN82129736, Austria) was also employed to evaluate the qualitative WFO conversion. The lower viscosity and higher peak integral values imply higher WFO conversion.[44,45] Therefore, the CCM calcination temperature for a high WFO conversion yielding catalyst was selected based on the above qualitative WFO conversion information.

The ^{1}H NMR analysis was performed for quantitative WFO conversion determination using a Bruker AVANCE TM 400 MHz NMR spectrometer. Deuterated chloroform ($CDCl_3$) and tetramethyl silicate were used as a solvent and internal standard, respectively.[46] The quantitative WFO conversion into methyl ester was determined by comparing methoxy protons of the methyl ester and α-methylene protons (eq 1).[47]

$$X = \left(\frac{2 \times A}{3 \times B}\right) \times 100\% \quad (1)$$

where X (%) is the conversion of triglycerides of WFO to its fatty acid methyl ester, A is the integral value of methoxy protons of methyl ester, and B is the integral value of the α-methylene protons of methyl ester.

RESULTS AND DISCUSSION

Oil Characterization. The acid value of the WFO was 1.56 mg KOH/g oil (i.e., % FFA as oleic acid = 0.78%). It is in the range of WFO acid value as reported by Sarno and Iuliano.[48] A solid gel was produced while transesterifying the WFO in this study with KOH may be due to its acid value (i.e., acid value > 1 mg_{KOH}/g_{oil}).[49] While utilizing the newly synthesized heterogeneous alkali catalysts, however, the problem was not noticed. The saponification value of the oil was 196.8 mg_{KOH}/g_{oil}, which is similar to that of waste palm frying oil reported somewhere.[50] Based on the empirical correlation,[51] the WFO molecular weight was determined to be 861.75 g/mol.

Proximate Analysis. The moisture, ash, volatile matter, and fixed carbon content of dried CH were 2.42 ± 0.02, 5.26 ± 0.21, 70.02 ± 0.25, and 22.32 ± 0.16% respectively. When it comes to obtaining catalysts from agricultural waste by calcination, the ash amount is crucial. The ash content of the CH in this study was near to the pineapple leaves (6%) and higher than cupuacu seeds (2.6%) ash contents.[35] The relation between the other proximate analysis values with LB ash-based catalysts physicochemical properties is not investigated. The volatile matter content of the CH ash (70.02 ± 0.25%) is an indicator for the potential of CH to be used as a source of bio-oil and biogas through pyrolysis and anaerobic digestion process, respectively.[52,53] High peak temperature can also be attained via the combustion of CH.[54] The fixed carbon content

https://doi.org/10.1021/acsomega.2c05572
ACS Omega 2022, 7, 45129−45143

of CH (22.32 ± 0.16%) makes CH a candidate precursor to biochar synthesis for the application of heterogeneous catalyst active site support[55] and soil fertility amendment.[56] After calcination of the CH (60 g) at 600 °C for 2 h, 17.83 g (29.72%) of ash and char mixture (A/C) was obtained. The mixture (A/C) contains 17.7% ash and 82.3% char. In the process of (A/C) preparation, energy can be extracted from CH combustion for power generation.[57] As a result, maximizing the energy extraction while also enhancing the A/C physicochemical characteristics for KNO_3 impregnation is crucial.

Thermal Analysis of Support and CCM. For A/C and CCM, a DSC thermogram in the range of 25−700 °C was generated (Figure 1). The early two endothermic peaks for

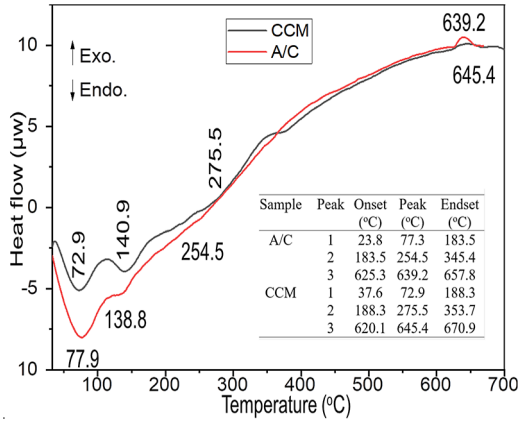

Sample	Peak	Onset (°C)	Peak (°C)	Endset (°C)
A/C	1	23.8	77.3	183.5
	2	183.5	254.5	345.4
	3	625.3	639.2	657.8
CCM	1	37.6	72.9	188.3
	2	188.3	275.5	353.7
	3	620.1	645.4	670.9

Figure 1. DSC thermogram of materials that contain ash and char mixture (A/C) and CCM.

both A/C and CCM correspond to the vaporization of water and impurities melting transition, respectively.[58,59] The decomposition of organic components induced endothermic peaks at 275.5 °C for CCM and 254.5 °C for A/C.[59] The melting of the impregnated KNO_3 in the CCM is responsible for the difference between the two thermograms in this region. The next region was due to the decomposition of inorganic constituents, mainly carbonates.[59] The exothermic peaks at 639.2 and 645.4 °C for A/C and CCM, respectively, are indicators of carbonated hydroxyapatite (CHAp) crystallization.[60] According to Kim et al. 2000,[61] the recrystallization of CHAp begins at about 600 °C, and then, the crystal size grows as temperature increases. The impregnation of KNO_3 onto A/C was shifted and broadened the CHAp crystallization peak (Figure 1). The CHAp crystallization peak temperature was shifted from 639.2 (A/C) to 645.4 °C (CCM) due to the impregnation of KNO_3 onto A/C. Peak broadening reveals the presence of impurity within the formed CHAp crystals.

Catalyst Synthesis Study. At first, KNO_3 impregnation was onto CH ash [synthesized by calcination of CH at 550 °C for 5 h to prepare a catalyst composite material (KNO_3/CHA)]. However, the calcination of KNO_3/CHA for 1 h at 650 °C resulted in a hard solid that was attached to the crucible and was not flowable due to agglomeration (Table 1). This phenomenon obliged changing the CCM synthesis method to KNO_3 impregnation onto ash and char mixture [KNO_3/(A/C)]. The hard solid aggregate formation was not detected while calcining the CCM. Fine powder solid catalysts were obtained from CCM calcination at 500, 550, 600, and 650 °C for 3 h. However, melting was observed approximately after 2 h calcination of CCM at 700 °C (Table 1). For A/C (without KNO_3 impregnation) calcination at 700 °C, the melting problem did not arise (Table 1, 700[b]). The reason for melting may be a reduced CCM melting point due to KNO_3 impregnation in addition to the possible CH thermal decomposition products (K_2O, Na_2O, and P_2O_5).[62] The product obtained after CCM calcination (catalyst) was observed to be heterogeneous in nature. A thin hard layer on the catalyst top surface was observed just after calcination (before homogenization with mortar and pestle) at 550 °C and higher calcination temperatures (Table 1). This layer may be formed by elements (K, Ca, and Na) volatilization and condensation and may resist the easy evacuation of gas products, protecting the CCM from easy combustion. Furthermore, CO_2 residence time could be increased which encourages its reaction with $Ca_{10}(PO_4)_6(OH)_2$ to form CHAp (Table 2i). Based on the physicochemical property evaluations and literature reports, possible reactions during the catalyst synthesis process are hypothesized (Table 2).

Effect of CCM Calcination Temperature on the Elemental Composition of Catalysts. The EDX results indicated that the catalysts contained metals such as K, Ca, Mg, Na, and Al (Table 3). The peaks for Au and Pd in the EDX spectra (Figure 2) were induced from the sputter layer. The elemental makeup of catalysts was highly altered with the CCM calcination temperature intensity change. Table 3 results

Table 1. Color Change of Catalysts Heated under Different CCM Calcination Temperatures

CCMCT (°C)	650[a]	500	550	600	650	700	700[b]
Ct[c] (h), conc. (wt.%)[d].	1, 25	3, 25	3, 25	3, 25	3, 25	2, 25	2, 0
Catalyst top surface before homogenization							
Homogenized catalyst	HAD[e]						

[a]KNO_3/CHA calcination. [b]Without KNO_3 impregnation. [c]Calcination time. [d]KNO_3 wt %. [e]Hard solid and cannot be homogenized.

https://doi.org/10.1021/acsomega.2c05572
ACS Omega 2022, 7, 45129−45143

Table 2. Summary of Proposed Reactions Takes Place during KNO_3 Impregnation onto Ash and Char Mixture (A/C) Sample and Calcination of Impregnated Ash and Char Mixture Sample (CCM) at Various Calcination Temperatures

	proposed reactions (rows a up to *k*)	during KNO_3 impregnation onto A/C (#)	during calcination of CCM at various temperatures (°C)					ref.
			500	550	600	650	700	
a	$MgCO_3 \rightarrow MgO + CO_2$	×	√	×	×	×	×	63
b	$FeS + O_2 \rightarrow Fe_3O_4 + Fe_2O_3 + SO_2$	×	√	×	×	×	√	63
c	$C + O_2 \rightarrow CO_2$	×	aLA	√	√	√	√	63
d	$CaCO_3 \rightarrow CaO + CO_2$	×	aLA	aLA	√	√	√	63, 64
e	$K_2CO_3 \rightarrow K_2O + CO_2$	×	×	aLA	√	√	√	64
f	$10Ca(OH)_2+3P_2O_5 \rightarrow Ca_{10}(PO_4)_6(OH)_2 + 9H_2O$	√	CR	CR	CR	CR	CR	61
g	$10CaCO_3 + 6H_3PO_4 \rightarrow Ca_{10}(PO_4)_6(OH)_2 + 10CO_2+8H_2O$	√	CR	CR	CR	CR	CR	65
h	$10Ca(OH)_2+6H_3PO_4 \rightarrow Ca_{10}(PO_4)_6(OH)_2 + 8H_2O$	√	CR	CR	CR	CR	CR	65
i	$Ca_{10}(PO_4)_6(OH)_2 + CO_2 \rightarrow Ca_{10}(PO_4)_6(OH)(CO_3) + H_2O$	×	×	×	×	√	×	60
j	$FeO + O_2 \rightarrow Fe_2O_3$	×	×	×	×	×	√	63
k	$Fe_3O_4 + O_2 \rightarrow Fe_2O_3$	×	×	×	×	×	√	63

×: the reaction didn't happen, aLA: the reaction is proceeding with a little amount, √: the reaction is taking place in a significant amount, CR: the reaction is completed below the stated temperature, #: during CCM preparation.

Table 3. Elemental Composition of Catalysts from SEM−EDX Analysis

	composition (wt %)											
catalyst	O	C	K	Ca	P	Mg	S	Cl	Na	Al	Pd	Au
C-25-500	51.26	38.21	8.25	1.44	0.33	0.28	0.13	0.09	0.00	0.00	0.00	0.00
C-25-550	64.5	9.51	18.33	4.39	1.92	0.59	0.45	0.22	0.09	0.00	0.00	0.00
C-25-600	61.92	8.68	24.24	3.10	0.77	0.98	0.30	0.00	0.00	0.00	0.00	0.00
C-25-650	64.7	10.22	21.21	1.99	0.25	1.66	0.00	0.00	0.00	0.00	0.00	0.00
C-25-700	61.62	6.72	25.91	3.55	1.16	0.02	0.47	0.29	0.13	0.12	0.00	0.00

show that the potassium (K) amount in the catalyst increased from 8.25 to 24.24 wt % as the CCM calcination temperature increased from 500 to 600 °C. However, an increase in the calcination temperature to 650 °C decreased the amount of K in the catalyst. This result is attributed to the formation of CHAp (Table 2i). Furthermore, calcination of CCM at 700 °C enhanced the decomposition of CHAp which results in an increase of K amount in the catalyst as compared to CCM calcination at 600 °C. Based on the elemental analysis of the catalyst K is the dominant metal in all calcination conditions (Table 3). In the previous studies also the dominant metal present was K in walnut shell,[26] Waste Musa paradisiacal plant,[29] and waste *M. indica* peels[28] ashes. For a step change of CCM calcination temperature from 500 to 550 °C, the carbon content of the catalyst decreased significantly (from 38.21 to 9.51%). This could be due to a combined effect of temperature changes and the carbon structure oxidative degradation due to KNO_3 decomposition.[66] The KNO_3 decomposition products may accelerate the combustion process. The increased C content for C-25-650 after continual decrement with temperature increment (Table 3) may be associated with carbonated hydroxyapatite formation and crystallization at 650 °C as stated during the DSC analysis.

Catalyst Color Change with CCM Calcination Temperature. The catalyst color change as a function of CCM calcination temperature was visible (Table 1). Additionally, the spectrophotometer's CIE $L^*a^*b^*$ values of color measurement were used to quantify the catalysts color intensity (Figure 3). According to the L^* values, the catalyst's brightness increased as the calcination temperature rose from 500 to 600 °C and maximum at 600 °C. The lower brightness at 500 °C was mostly owing to the presence of more carbon material (Table 3). The carbon combustion (Table 2c) increased the brightness, and further temperature increments to 650 and 700 °C lowered the catalyst brightness, possibly due to the increased yellow and red color intensity (b^* and a^* values, respectively). The b^* intensity rise with CCM calcination temperature was possibly due to the increased K_2O (pale yellow color) amount because of potassium compounds decomposition. When compared to the C-25-700 catalyst, the yellow color intensity decrement for C-00-700 indicates that KNO_3 caused more K_2O formation. The red color intensity also increased with temperature and reached the maximum at 700 °C (for CCM calcination). The formation of carbonated hydroxyapatite crystals could also be a factor in the color intensity changes. The rise in red color intensity may also be due to the formation of iron oxide (Fe_2O_3) from the reaction of a trace amount of iron compounds with oxygen (Table 2j,k).[63] The C-00-700 was less bright than the C-25-700, with a reduction in red and yellow color intensity, implying that the lack of KNO_3 resulted in less carbon material combustion.

XRD Analysis. The XRD patterns of A/C, CCM, C-00-600, C-25-600, and C-25-650 (Figure 4) were compared to ash catalyst XRD patterns in the reported literature. One of the significant differences between A/C and CCM with the catalysts was the absence of the XRD hump of the amorphous framework from the catalysts XRD pattern. The incorporation of potassium nitrate (KNO_3) into A/C was recognized by XRD peak 2θ values at 23.74, 33.88, and 41.1 for CCM. However, the KNO_3 peak was not visible in the XRD patterns of the catalysts may be due to KNO_3 conversion into K_2O.[32] The K_2O peaks are visible in the XRD patterns of the catalysts. XRD peaks appeared around the 2θ value of 52.3 which do not

https://doi.org/10.1021/acsomega.2c05572
ACS Omega 2022, 7, 45129−45143

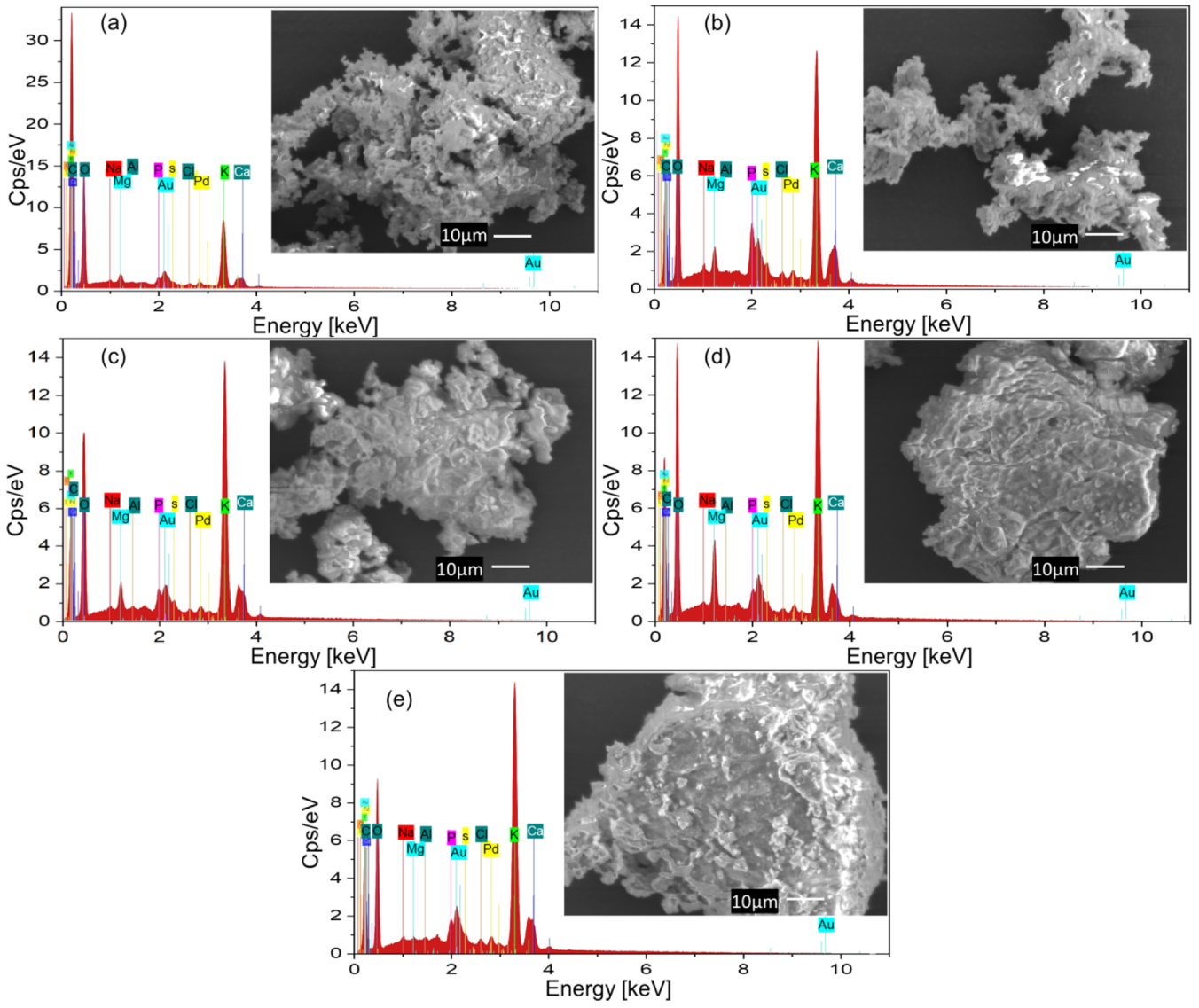

Figure 2. SEM−EDX analysis of catalysts obtained at various calcination temperatures: (a) C-25-500, (b) C-25-550, (c) C-25-600, (d) C-25-650, and (e) C-25-700 catalysts.

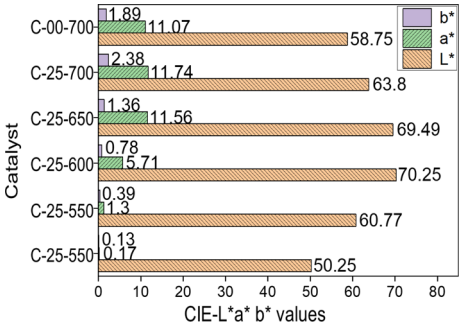

Figure 3. Color analysis of catalyst obtained at different calcination temperatures using spectrophotometry.

occur in the XRD pattern of the catalysts, revealing the presence of carbon molecules in A/C and CCM.[28] In addition to K_2CO_3, the strongest peak at 32.28 for the C-25-650 catalyst also belongs to the carbonated hydroxyapatite crystals.[67] The absence of fairchildite [$K_2Ca(CO_3)_2$] crystal peaks in the CCM XRD pattern could be due to fairchildite transitioning to butschliite and subsequently leaching to calcite during KNO_3 impregnation. No $CaCO_3$ peaks were observed for C-00-600 and C-25-600 catalysts. This happened may be due to $CaCO_3$ conversion into CaO (i.e., the decomposition temperature of $CaCO_3$ decreases in the presence of K_2CO_3[64]) or to hydroxyapatite (Table 2g). The kaolinite [$Al_2Si_2O_5(OH)_4$] crystal peak (around 2θ values of 24) disappearance for C-25-650 was due to its conversion to an amorphous metakaolin.[37] The $CaCO_3$ peak was seen in the C-25-650 XRD pattern due to the adsorption of CO_2 from the atmosphere by CaO. The intensity of major peaks increased except for fairchildite when comparing the XRD pattern of KNO_3 modified and unmodified catalysts (C-00-600 and C-25-600). As stated in the literature, the increased intensity, and narrowed diffraction peaks are indicators of increased crystallinity and crystal size.[68] One of the positive impacts of KNO_3 was the enhanced crystallinity (high crystallinity can sometimes be a sign of increased catalyst activity[18]). However, somewhere stated that the crystal size has an impact on catalysts BET surface area.[69] Because of carbonate substitutions (during CHAp formation) in the hydroxyapatite lattice (lattice strain), the X-ray

https://doi.org/10.1021/acsomega.2c05572
ACS Omega 2022, 7, 45129−45143

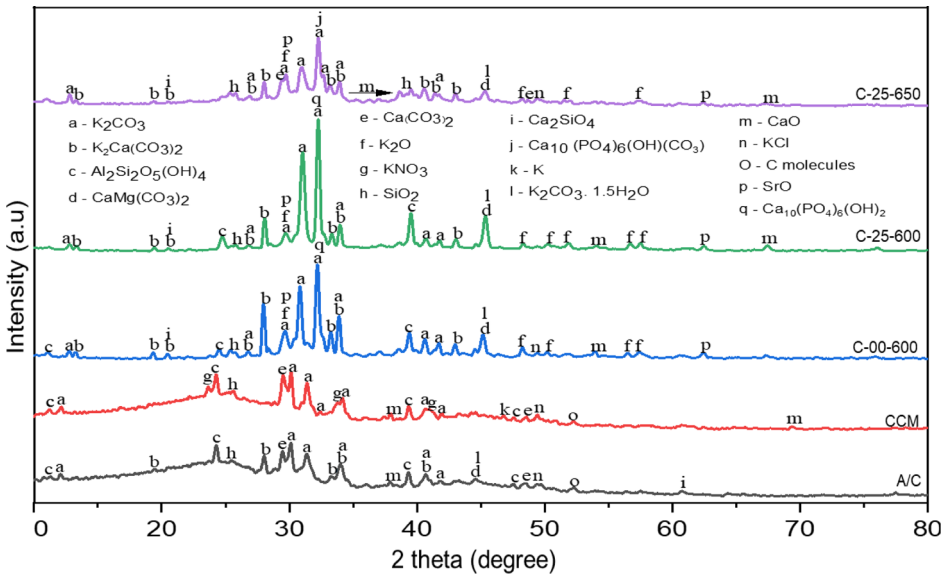

Figure 4. Comparison of XRD patterns of the mixture of ash and char (A/C), KNO_3-impregnated A/C (CCM), and catalysts obtained from A/C (C-00-600) and CCM (C-25-600 and C-25-650).

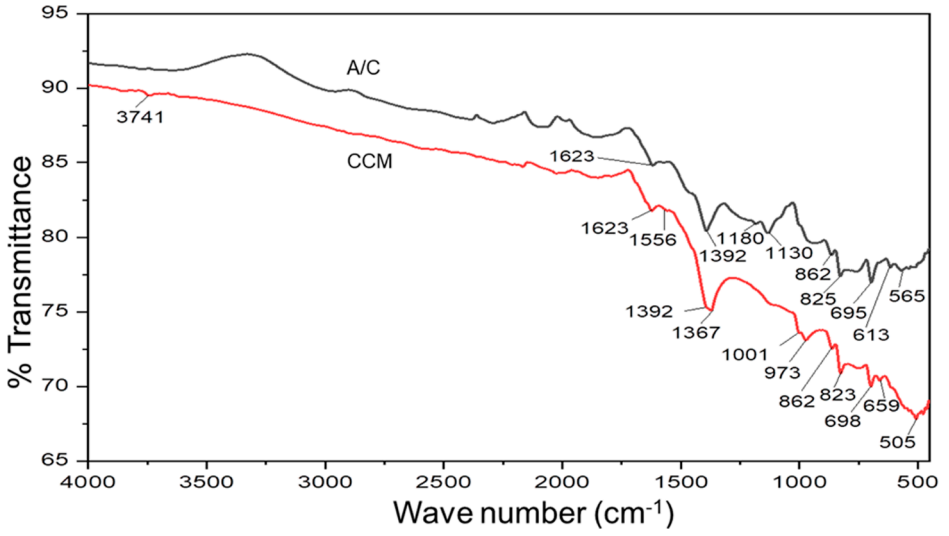

Figure 5. FTIR spectra of the mixture of ash and char (A/C) and KNO_3 impregnated A/C (CCM).

diffraction peaks of C-25-650 particles are broader and shorter than those of C-25-600 particles, indicating its weaker crystallinity and small crystal size.[67]

Peaks of XRD pattern for C-25-600 (the catalyst that yielded higher WFO conversion) were assigned to their corresponding compounds as follows. At a 2θ value of 25.84, peaks for SiO_2 appeared. The K_2O peaks were observed at 48.32, 50.34, 51.88, 56.76, and 57.54. The peaks at 13.23, 19.48, 20.54, 26.86, 28.06, 33.36, 34.00, and 43.06 belong to $K_2Ca(CO_3)_2$.[25] The presence of the K_2CO_3 was revealed by the XRD peaks at 2θ values of 12.80, 26.86, 29.78, 31.04, 32.28, 34.00, 40.80, and 41.80. Diffraction peaks at 54.22 and 67.44 were due to the CaO presence. Alkali oxides SrO and MgO revealed their existence by inducing XRD peaks at 2θ values of 29.78 and 62.5. Hydrated potassium carbonate ($K_2CO_3{\cdot}1.5H_2O$) was also realized based on a similar 2θ value (45.30) reported by Olatundun et al.[25] Basumatary, et al. (2021) reported comparable 2θ values for K_2CO_3, K_2O, and KCl in the banana trunk, peel, and rhizome ash catalysts.[29] The study by Miladinović et al.[26] on a walnut shell catalyst was also considered in assigning 2θ values for SiO_2, CaO, MgO, and K_2O. Nath et al.[36] also reported equivalent 2θ values of CaO, KCl, K_2O, and SrO. During the allocation of 2θ values of SiO_2, CaO, and KCl, a report by Basumatary et al.[70] for heterogeneous catalyst synthesized from sugarcane bagasse was also utilized. A catalyst from waste *M. indica* peel ash had also similar 2θ values of SiO_2 and CaO.[28] The presence of hydroxyapatite crystals was recognized based on the report by Pavankumar et al.[67] Finally, from the XRD analysis, it was observed that potassium (K) and calcium (Ca) were the abundant components in the form of their oxide, chloride, and carbonate form and played a role in the transesterification of the WFO. The presence of $K_2CO_3{\cdot}1.5H_2O$ and $K_2Ca(CO_3)_2$ suggests the ash's high catalytic potential.[25]

FTIR Analysis. Comparative examination of CCM and A/C FTIR spectra was used to look into functional group identification and alterations caused by KNO_3 impregnation (Figure 5). The peaks at 1623 (C═C) indicate the presence of

https://doi.org/10.1021/acsomega.2c05572
ACS Omega 2022, 7, 45129−45143

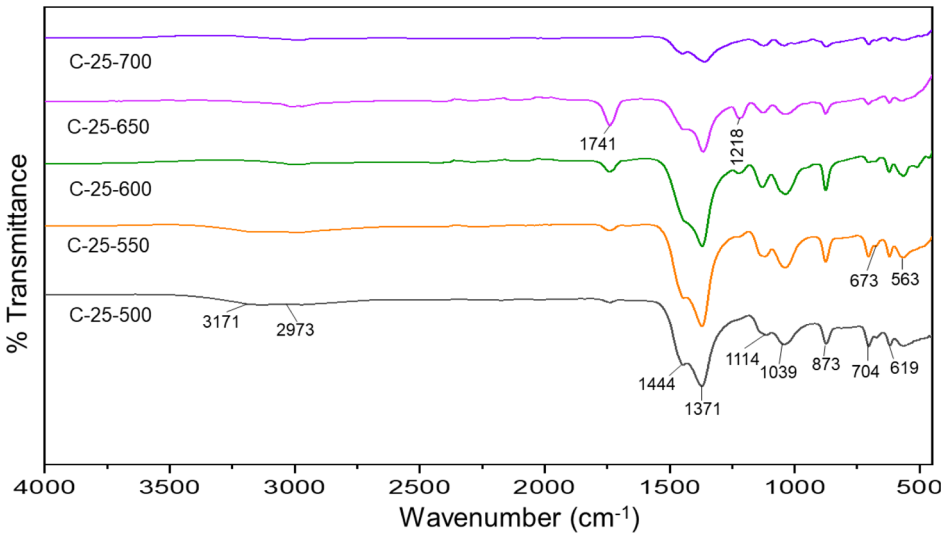

Figure 6. FTIR spectra of catalysts obtained from the calcination of impregnated A/C at different calcination temperatures.

aromatic groups.[71] The incorporation of KNO_3 to the A/C was recognized by the new peaks at 1556 and 1367 (N−O vibrations) for CCM.[32] The bands at 862 and 867 belong to CO_3 group bending[39] and 823, 698, 695, 825, 613, and 565 for A/C and CCM are due to metal−O stretching vibrations.[29] The vibration at 3741 for CCM was due to OH stretching vibration in the amorphous hydroxyapatite structure.[60] The presence of the phosphate group was recognized by P═O and P−O bond stretching vibrations at 1180 and 1130, respectively, for A/C.[72] These two bands migrated to 1001 and 973, which correspond to the triply degenerate asymmetric and nondegenerate symmetric stretching modes of PO_4^{3-} (P−O bond), respectively, due to the possibility of the amorphous hydroxyapatite formation (Table 2f−i).[60]

The catalysts prepared at different calcination temperatures have similar FTIR spectrum patterns with a few differences (Figure 6). The broad peak between 3485 and 2645 for catalysts was due to the stretching mode of OH ions of adsorbed water. The band at 2973 belongs to C−H stretching because of organic constituents.[73] Due to KNO_3 breakdown, the N−O stretching band is not visible in the catalysts FTIR spectra.[32] Peaks due to the bending mode of O−H−O of lattice water appeared in 1741[74] and the intensity increased with temperatures between 500 and 650 °C. However, it disappeared at 700 °C due to dehydroxylation.[60] Dehydroxylation of carbonated hydroxyapatite (CHAp) at 700 °C was also stated elsewhere.[75] The presence of carbonates was identified by their C−O stretching and bending vibrations peaks at 1444 and 1371, respectively.[29] These C−O stretching bands decrease in intensity with temperature due to the decomposition reaction of carbonates. The bands at 1114 and 1039 correspond to the stretching vibration mode of the phosphate group in hydroxyapatite.[73] Metal−oxygen vibratory stretching peaks appeared at 563, 619, and 704 due to oxides (K_2O, CaO, and MgO) and carbonates which are responsible for facilitating the transesterification reaction.[25,29] Peaks at 563 and 619 are may also characteristic vibrational modes of the phosphate group.[73] The CO_3 group was identified by its characteristic bending peak at 871.[39]

BET Surface Area Analysis. It was realized that the BET surface area is inversely proportional to the CCM calcination temperature (Table 4). The highest surface area was for the C-25-500 catalyst. The reduced surface area, when compared to catalysts from previous studies (Table 4), is probably due to pore blockage by particle agglomeration and sintering. The crystal size growth of the catalyst (C-25-600 from XRD analysis) may also initiate pore blockage and reduced the BET surface area.[69] There was difficulty in determining the BET surface area of the C-25-650 catalyst may be due to its morphology (Figure 7). Because of the stated reason, the surface area may become below the threshold of the sensitivity of the surface area analyzer.

Table 4. Comparison of BET Surface Area and Basicity of the Catalysts with Previous Works

catalyst name	BET surface area (m^2/g)	total basicity (mmol/g)	leachable basicity (mmol/g)	ref.
C-25-500	2.251	0.75	3.11	this work
C-25-550	2.132	0.93	3.50	
C-00-600	n.d[a]	1.05	3.32	
C-25-600	0.773	1.6	3.93	
C-25-650	n.d[a]	1.93	3.94	
C-25-700	0.585	2.9	4.21	
walnut shell ash	8.8			26
waste *Sesamum indicum* plant ash	3.66			36
M. paradisiaca peel ash	4.1	1.43		29
trunk ash	6.4	1.59		
rhizome ash	7.0	1.39		
$Mg_9Al_1(10)$		0.51	0.21	40
$Mg_8Zn_1Al_1$		0.13	4.28	

[a]Not determined.

Basicity Analysis. The total basicity (TB) and leachable basicity (LB) values increased with calcination temperature (Table 4). The TB values are close to the values reported for ash and synthetic mixed oxide base catalysts (Table 4). In all cases, the TB is lower than leachable basicity because of catalysts very low surface area (<3 m^2/g). A catalyst with a low surface area masks the alkali sites inside the structure and prevents toluene titration, whereas water washing allows those sites to be leached.[40] Therefore, the increase in TB with calcination temperature was due to an alkaline site

https://doi.org/10.1021/acsomega.2c05572
ACS Omega 2022, 7, 45129−45143

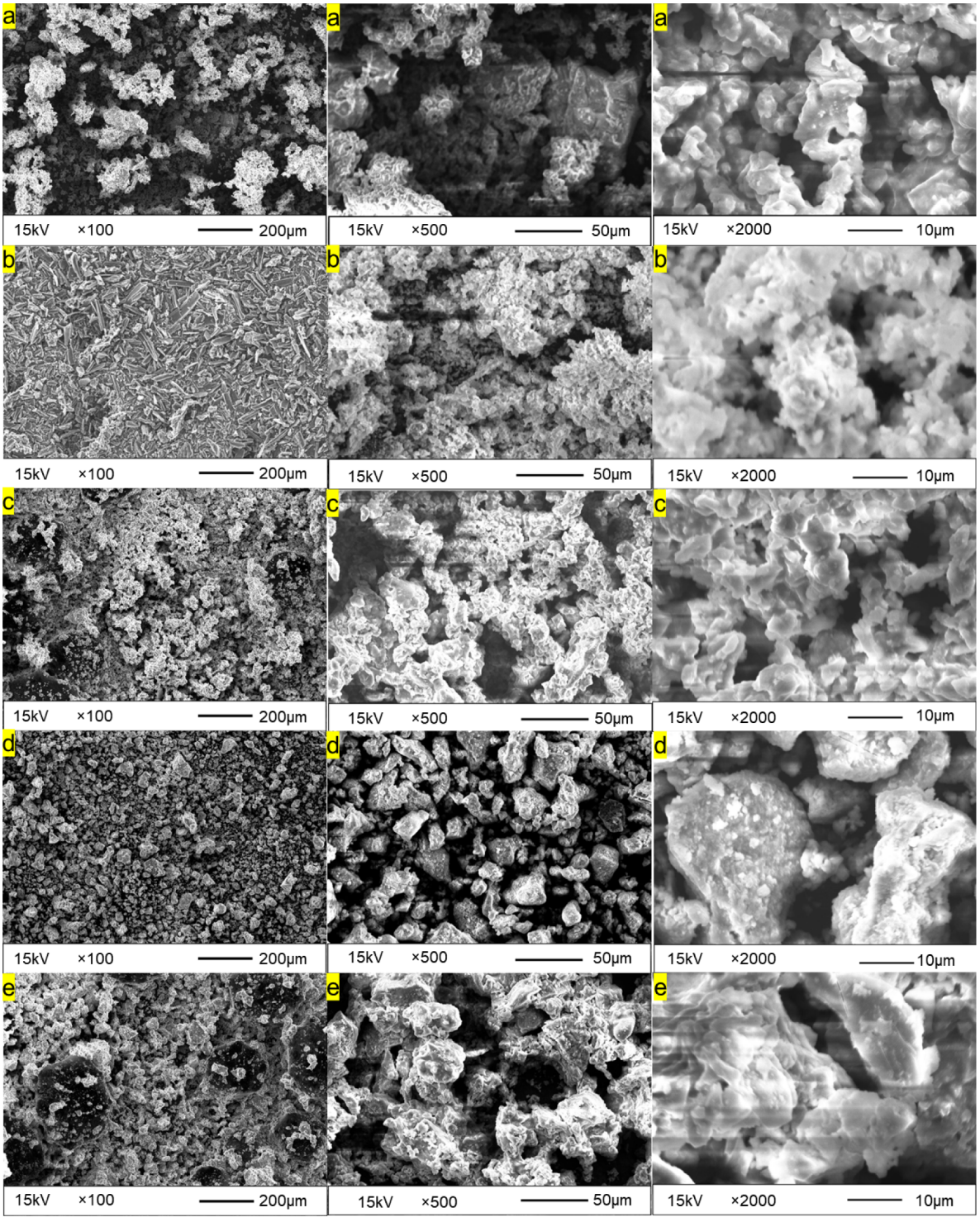

Figure 7. SEM micrograph of (a) ash and char mixture (A/C) calcined at 600 °C (C-00-600) and KNO_3 impregnated A/C calcined at different temperatures and (b) C-25-550, (c) C-25-600, (d) C-25-650, and (e) C-25-700 observed at different magnifications.

concentration increment on the catalyst surface. However, for higher FFA-containing feedstock, high basic site presence on a catalyst surface will reduce the biodiesel yield.[15] The lower biodiesel yield for the C-25-700 catalyst may be associated with these phenomena in addition to its BET surface area. The increase in leachable basicity with the calcination temperature was due to carbonate decomposition to their corresponding highly water-soluble alkali oxides such as CaO and K_2O.[64] The carbonate decomposition at lower calcination temperature was may be facilitated due to the presence of carbon for K_2CO_3 and K_2CO_3 for $CaCO_3$ in the CCM.[64,76] The KNO_3 modification may boost the catalyst basicity in two ways: that is, by facilitating the K_2CO_3 and $CaCO_3$ decomposition and by acting as a source of K_2O during its decomposition.

Catalyst Morphology Analysis. For each CCM calcination temperature, different morphological structures were observed in the SEM image (Figure 7). The highly porous C-25-550 catalyst, with a particle size of 200 μm, had a unique flake

https://doi.org/10.1021/acsomega.2c05572
ACS Omega 2022, 7, 45129−45143

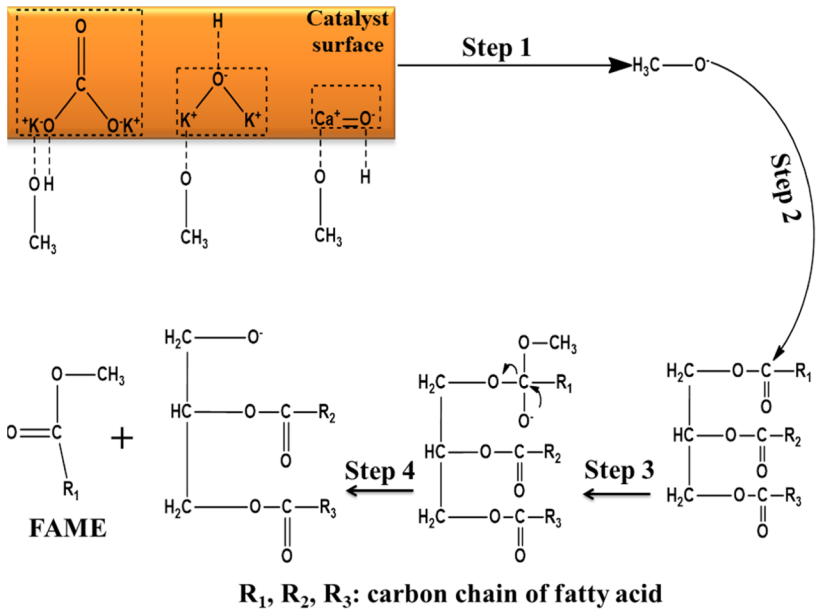

Figure 8. KNO_3-loaded CH catalytic transesterification proposed reaction mechanism of WFO.

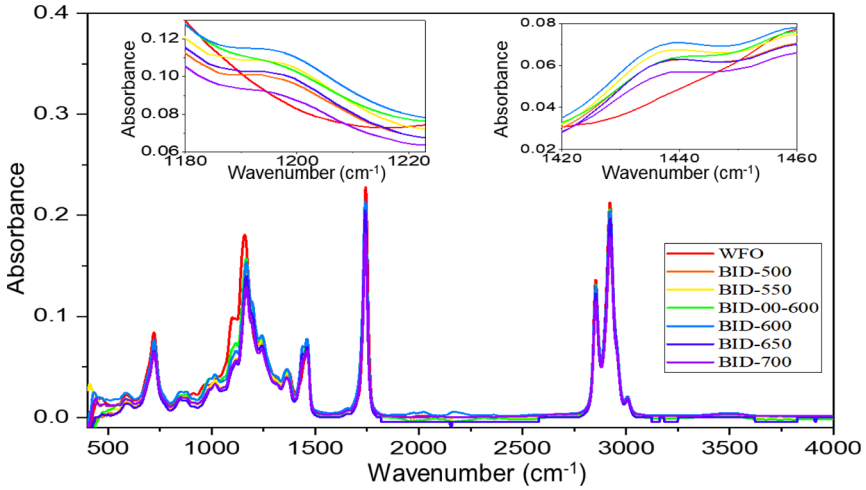

Figure 9. FTIR spectra of WFO and biodiesel synthesized using calcined ash and char mixture (A/C) and impregnated A/C and their FTIR spectra expansion within the region of 1180−1220 cm^{-1} (top left corner) and 1420−1460 cm^{-1} (top right corner).

morphology due to pore opening (Figure 7b). The pore opening is caused by oxidative carbon structural (i.e., aliphatic groups) degradation, as indicated by the higher carbon content difference between C-25-500 and C-25-550 in the EDX analysis (Table 3). Pore opening was also observed in biochar activated with an oxidizing agent H_2O_2.[66] The morphology of C-00-600 (Figure 7a) and C-25-600 (Figure 7c) at a particle size of 200 μm is also porous. The effect of KNO_3 impregnation was exposed by the reduced porosity of C-25-600 when compared to C-00-600. The C-25-650 (Figure 7d) particles were the most tightly packed and large agglomerates among the catalysts may be due to sintering.[64] Agglomeration may also be associated with CHAp crystallization.[77] Most of the particles in C-25-650 are large and have nonporous surfaces. The formation of large particles reduces the catalyst surface area significantly. Increasing the calcination temperature from 650 to 700 °C partially recovered the spongy morphology of the catalyst, which may be related to structural and compositional changes.[26] There is a close similarity between the morphology of the C-25-600 and ash catalyst from Cocoa pod husk-plantain peel blend, especially at a particle size of 10 μm.[29]

Catalyst Performance Test. Figure 8 shows the proposed reaction mechanism for the newly synthesized heterogeneous basic catalyst during triglyceride transesterification. In the first step, methoxides are formed by the interaction of methanol mainly with K_2CO_3, K_2O, and CaO which acts directly as a strong nucleophile. The methoxide attacks the carbonyl group of the triglyceride in step 2 to generate a tetrahedral reactive intermediate (step 3). In step 4, the intermediate product is converted into 1 mol of fatty acid methyl ester and diglyceride anion.[78] Then, the transesterification reactions continue with the reaction of diglyceride and monoglyceride with other methoxide molecules to form 2 mol of fatty acid methyl ester (FAME). The diglyceride and monoglyceride anions are neutralized by the proton on the catalyst surface to form a glycerol molecule.

https://doi.org/10.1021/acsomega.2c05572
ACS Omega 2022, 7, 45129−45143

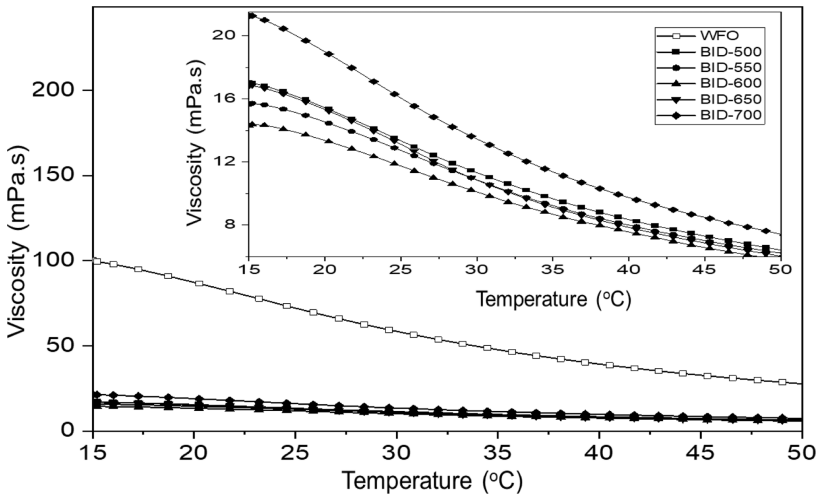

Figure 10. Effect of temperature and catalyst type used for transesterification reaction of WFO on the viscosity of produced biodiesel.

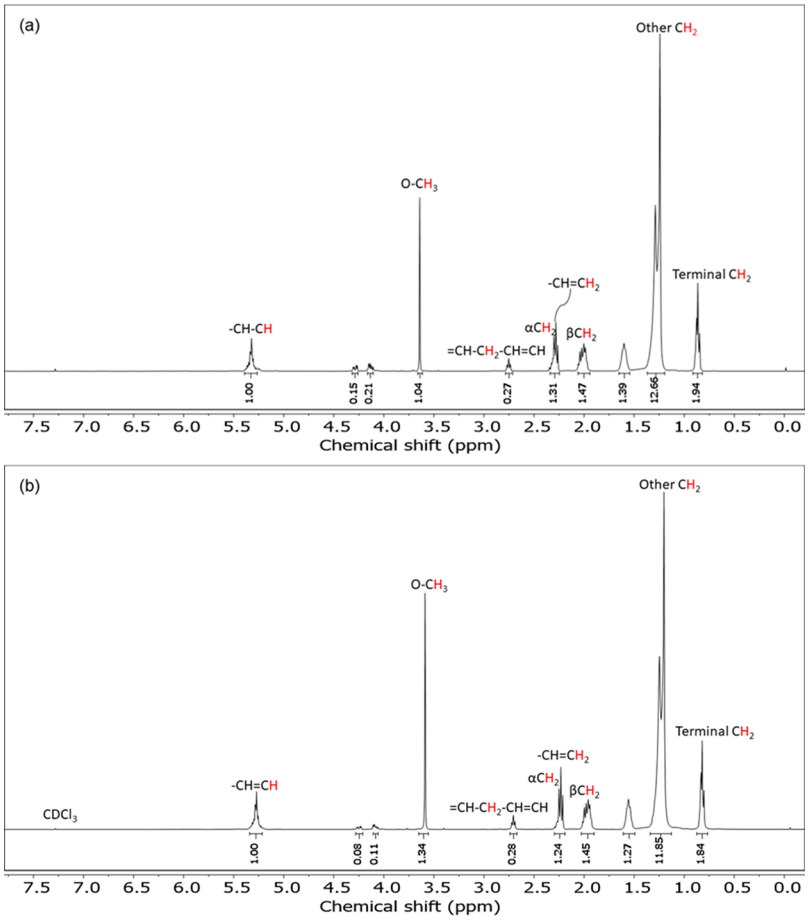

Figure 11. ^{1}H NMR spectra synthesized biodiesel obtained by transesterification reaction using calcined: ash and char mixture (A/C) [BID-00-600 (a)] and impregnated A/C [BID-600 (b)].

The regions 1425−1447 cm^{-1} (top right corner, CH_3 asymmetric bending) and 1188−1200 cm^{-1} (top left corner, O−CH_3 stretching) were absent in oil but present in biodiesel (Figure 9). During the qualitative biodiesel yield analysis, the peak integral values within the 1188−1200 cm^{-1} region were used. A maximum peak integral value of 0.38 was obtained for BID-600. The peak integral value for biodiesel produced using a catalyst without KNO_3 modification (BID-00-600) was 0.27. This implies that the KNO_3 modification had a positive effect on the catalyst activity. The qualitative WFO conversion was also analyzed using biodiesel viscosity measurement (Figure 10). Higher oil conversion implies lower biodiesel viscosity. The lowest viscosity was for BID-600. At 40 °C the viscosity of WFO and BID-600 were 38.56 and 7.46 mPa s, respectively. This was also evidence for WFO conversion into a mixture of fatty acid methyl ester (biodiesel). The lower viscosity value for BID-600 implies the higher activity of the C-25-600 catalyst.

https://doi.org/10.1021/acsomega.2c05572
ACS Omega 2022, 7, 45129−45143

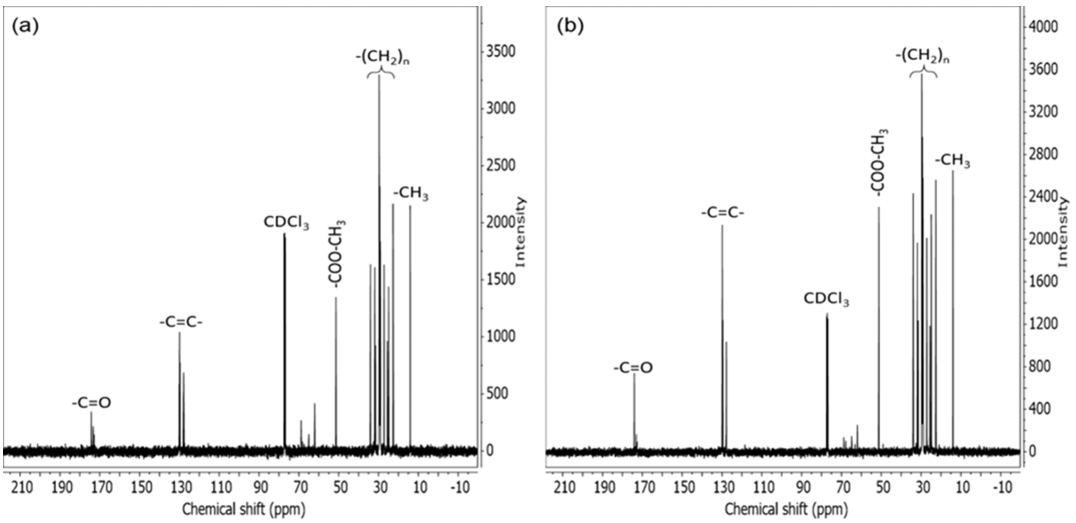

Figure 12. ^{13}C NMR spectra of synthesized biodiesel obtained by the transesterification reaction using calcined ash and char mixture (A/C) [BID-00-600 (a)] and impregnated A/C [BID-600 (b)].

Table 5. Comparison of Catalytic Activity of KNO_3-Loaded CH Ash Catalyst with Reported Solid Alkali Catalysts for Transesterification Reaction

		reaction conditions					
catalyst	feedstock	temp. (°C)	catalyst amount (wt %)	methanol to oil molar ratio	time (h)	FAME yield (wt %)	ref.
C-25-600	WFO	45	3	12:1	1	72.04	this work
CaO derived from *Mereterix mereterix*	used oil	60	3	6.03:1	3	89	30
CaO/SCBA[a]	Jatropha seed oil	65	10	9:1	4.75	92.84	70
KNO_3/(CaO−MgO)	Neem seed oil	50−55	0.9	12:1	24	78	31
KNO_3/Al_2O_3	Jatropha seed oil	70	6	12:1	6	84	41

[a]SCBA: sugar cane bagasse ash.

Both viscosity and FTIR peak integral analysis confirmed the higher activity of the C-25-600 catalyst. The catalysts activity was in the order of C-25-600 > C-25-550 > C-25-650 > C-25-500 > C-25-700. Therefore, a CCM calcination temperature of 600 °C was selected for the catalyst synthesis.

Analysis of WFO Methyl Ester Using ^1H NMR. The ^1H NMR spectrum for biodiesel produced using a catalyst without KNO_3 modification of the CH ash (BID-00-600) and with KNO_3 modified CH ash (BID-600) are presented in (Figure 11a) and (Figure 11b), respectively. The peaks were identified by their corresponding integral values (at the bottom of the peaks) and chemical shifts. At a chemical shift of 2.24 to 2.28 and 2.19 to 2.23 biodiesel characteristic peaks [α-methylene protons adjacent to the carbonyl carbon to esters ($-CH_2-CO_2R$)] were observed with an integral value of 1.31 and 1.24. The singlet sharp peaks with integration values of 1.04 and 1.34 during a chemical shift at 3.62 and 3.57 ppm were due to methoxy ($-CO-O-CH_3$) protons that indicated the biodiesel formation. The quartet characteristics peaks designated by integral values of 1.00 correspond to olefinic protons ($-CH=CH-$). At a chemical shift of 2.73 and 2.69 ppm, a triplet with integral values of 0.27 and 0.28 was due to bisallylic ($-C=C-CH_2-C=C-$) groups of unsaturated fatty acids. The carbonyl carbon β-methylene protons ($-CH_2-C-CO_2R$) appearance was recognized by their triplet with integral values of 1.47 and 1.45. Signals between 4.08 and 4.28 ppm (glycerol moiety protons of the WFO) are due to incomplete conversion of triglycerides to fatty acid methyl ester.[79]

According to eq 1, the WFO conversion from ^1H NMR analysis for BID-00-600 and BID-600 were 52.92 and 72.04%, respectively. It was a 19.12% conversion difference. Both the ^1H NMR and FTIR analysis confirmed that the modified CH catalyst (C-25-600) has better performance than the unmodified one (C-00-600). The difference in WFO conversion was from the enhanced basicity and crystallinity of the CH ash because of its modification with KNO_3.

The ^{13}C NMR spectra of BID-00-600 and BID-600 are presented in Figure 12a,b, respectively. The ^{13}C NMR spectrum exhibits signals at 62.20, 69.10 ppm (Figure 12a), and 61.65, 68.67 ppm (Figure 12b), which are respectively attributed to the unconverted WFO and the methylene and methine carbons of the glycerine moiety. The methoxy carbon ($-COO-CH_3$) of the methyl esters signal appeared at 51.10 ppm for both spectra, confirming the conversion of the WFO into biodiesel. On the other hand, the olefinic carbons contained in the biodiesel were indicated by the signals at 127.62−129.71 ppm in the ^{13}C NMR spectra of BID-00-600 and 127.67−129.91 ppm in the ^{13}C NMR spectra of BID-600. In the ^{13}C NMR study, signals at 172.31, 173.01, and 174.10 ppm (Figure 12a), and 172.45, 172.73, and 173.71 ppm (Figure 12b) also appeared. In both spectra, the first two signals are due to the carbonyl carbon of the triglyceride and the third ones are because of the carbonyl carbon of biodiesel. The signals at 22.31−33.72 ppm (Figure 12a) and 22.5−33.83 ppm (Figure 12b) and 13.62 (Figure 12a) and 13.79 ppm (Figure 12b) ppm are indicating the methylene and methyl

https://doi.org/10.1021/acsomega.2c05572
ACS Omega 2022, 7, 45129−45143

carbons of the fatty acid moiety of biodiesel, respectively. The ^{13}C NMR spectrum signal intensity that belongs to biodiesel carbon was higher for BID-600 than BID-00-600 and the reverse is true for triglyceride carbon signals. This implies that the WFO conversion is higher when using the C-25-600 catalyst than C-00-600 during the WFO transesterification.

Comparison of KNO_3-Loaded CH Ash Catalyst with Other Catalysts. Table 5 presents a comparison of the synthesized catalyst with some reported heterogeneous catalysts. Although the biodiesel yield achieved with other catalysts in Table 5 was higher than the yield achieved in the current study, the reaction conditions were higher. When using KNO_3-loaded CH catalyst, 72.04 wt % yield of biodiesel was obtained at a lower temperature and in a shorter reaction time as compared to other reported catalysts (Table 5). Therefore, the synthesized catalyst has promising potential in the transesterification reaction to produce biodiesel.

CONCLUSIONS

CH's potential as a precursor in the synthesis of a heterogeneous alkali catalyst for the transesterification of WFO was revealed in this study. The activity of the catalyst was highly dependent on the CCM calcination temperature. Maximum WFO conversion (72.04%) was attained at a calcination temperature of 600 °C. Lower WFO conversions below and above 600 °C CCM calcination temperatures were due to lower basicity and reduced surface area of catalysts, respectively. The combined effect of morphology, crystallinity, and basicity, all of which were highly influenced by the calcination temperature, determined the activity of the catalysts. Increasing the calcination temperature increased the catalyst basicity because of the thermal decomposition of compounds into their corresponding oxides (mainly K_2O and CaO). However, the rise in the CCM calcination temperature reduced the catalyst surface area due to the melting and sintering. The KNO_3 impregnation (modification) affected the basicity and morphology of the catalysts. It also had a significant role in altering the catalyst crystallinity. When compared to the unmodified catalyst (C-00-600), the modified catalyst (C-25-600) increased the WFO conversion by 19.12%. Furthermore, the transesterification reaction parameters optimization and reusability of the produced catalyst investigation are in progress.

AUTHOR INFORMATION

Corresponding Author

Nurelegne Tefera Shibeshi − *School of Chemical and Bio-Engineering, Addis Ababa Institute of Technology, Addis Ababa University, Addis Ababa 1176, Ethiopia;* orcid.org/0000-0002-4387-4889; Phone: +251911607185; Email: nurelegne.tefera@aait.edu.et

Authors

Demelash Tilahun Bekele − *Department of Chemical Engineering, College of Biological and Chemical Engineering, Addis Ababa Science and Technology University, Addis Ababa 16417, Ethiopia;* orcid.org/0000-0002-4118-6759

Ali Shemsedin Reshad − *Department of Chemical Engineering, College of Biological and Chemical Engineering, Addis Ababa Science and Technology University, Addis Ababa 16417, Ethiopia; Center of Excellence for Sustainable Energy Research, Addis Ababa Science and Technology University, Addis Ababa 16417, Ethiopia;* orcid.org/0000-0003-3695-954X

Complete contact information is available at: https://pubs.acs.org/10.1021/acsomega.2c05572

Notes

The authors declare no competing financial interest.

ACKNOWLEDGMENTS

The authors would like to express their special thanks to the Chemical and Food Process Engineering laboratories Under Chemical Engineering Department, Addis Ababa Science and Technology University, Ethiopia for providing various analytical facilities and sample analysis. Furthermore, the first author would like to thank Addis Ababa Science and Technology University for giving fellowship opportunity for Ph.D. study.

REFERENCES

(1) Mofijur, M.; Rasul, M. G.; Hassan, N. M. S.; Nabi, M. N. Recent Development in the Production of Third Generation Biodiesel from Microalgae. *Energy Proc.* **2019**, *156*, 53−58.

(2) Ramos, M.; Dias, A. P. S.; Puna, J. F.; Gomes, J.; Bordado, J. C. Biodiesel Production Processes and Sustainable Raw Materials. *Energies* **2019**, *12*, 4408.

(3) Khan, M. I.; Chhetri, A. B.; Islam, M. R. Analyzing Sustainability of Community-Based Energy Technologies. *Energy Sources B: Econ. Plan. Policy.* **2007**, *2*, 403−419.

(4) Mohamed, M. A. Biofuel Production from Used Cooking Oil Using Pyrolysis Process. *Int. J. Res. Appl. Sci. Eng. Technol.* **2017**, *V*, 2971−2976.

(5) Bhuiya, M. M. K.; Rasul, M. G.; Khan, M. M. K.; Ashwath, N.; Azad, A. K.; Hazrat, M. A. Second Generation Biodiesel: Potential Alternative to-Edible Oil-Derived Biodiesel. *Energy Proc.* **2014**, *61*, 1969−1972.

(6) Lin, L.; Cunshan, Z.; Vittayapadung, S.; Xiangqian, S.; Mingdong, D. Opportunities and Challenges for Biodiesel Fuel. *Appl. Energy* **2011**, *88*, 1020−1031.

(7) Demirbas, A.; Bafail, A.; Ahmad, W.; Sheikh, M. Biodiesel Production from Non-Edible Plant Oils. *Energy Explor. Exploit.* **2016**, *34*, 290−318.

(8) Fukuda, H.; Kondo, A.; Noda, H. Biodiesel Fuel Production by Transesterification of Oils. *J. Biosci. Bioeng.* **2001**, *92*, 405−416.

(9) Chen, Y. C.; Lin, D. Y.; Chen, B. H. Metasilicate-Based Catalyst Prepared from Natural Diatomaceous Earth for Biodiesel Production. *Renewable Energy* **2019**, *138*, 1042−1050.

(10) Mohamed, R. M.; Kadry, G. A.; Abdel-Samad, H. A.; Awad, M. E. High Operative Heterogeneous Catalyst in Biodiesel Production from Waste Cooking Oil. *Egypt. J. Pet.* **2020**, *29*, 59−65.

(11) Biernat, K.*Biofuels—State of Development*; Biernat, K., Ed.; InTech, 2018.

(12) Catarino, M.; Ferreira, E.; Soares Dias, A. P.; Gomes, J. Dry Washing Biodiesel Purification Using Fumed Silica Sorbent. *Chem. Eng. J.* **2020**, *386*, 123930.

(13) Bedir, Ö.; Doğan, T. H. Use of Sugar Industry Waste Catalyst for Biodiesel Production. *Fuel* **2021**, *286*, 119476.

(14) Yaşar, F. Biodiesel Production via Waste Eggshell as a Low-Cost Heterogeneous Catalyst: Its Effects on Some Critical Fuel Properties and Comparison with CaO. *Fuel* **2019**, *255*, 115828.

(15) Abnisa, F.; Sanni, S. E.; Alaba, P. A. Comparative Study of Catalytic Performance and Degradation Kinetics of Biodiesels Produced Using Heterogeneous Catalysts from Kaolinite. *J. Environ. Chem. Eng.* **2021**, *9*, 105569.

(16) Védrine, J. C. Heterogeneous Catalysis on Metal Oxides. *Catalysts* **2017**, *7*, 341.

https://doi.org/10.1021/acsomega.2c05572
ACS Omega 2022, 7, 45129−45143

(17) Bedir, Ö.; Doğan, T. H. Comparison of Catalytic Activities of Ca-Based Catalysts from Waste in Biodiesel Production. *Energy Sources A: Recovery Util. Environ. Eff.* **2021**, 1−18.
(18) Refaat, A. A. Biodiesel Production Using Solid Metal Oxide Catalysts. *Int. J. Sci. Environ. Technol.* **2011**, *8*, 203−221.
(19) Taufiq-Yap, Y. H.; Teo, S. H.; Rashid, U.; Islam, A.; Hussien, M. Z.; Lee, K. T. Transesterification of Jatropha Curcas Crude Oil to Biodiesel on Calcium Lanthanum Mixed Oxide Catalyst: Effect of Stoichiometric Composition. *Energy Convers. Manag.* **2014**, *88*, 1290−1296.
(20) Xie, W.; Wang, H.; Li, H. Silica-Supported Tin Oxides as Heterogeneous Acid Catalysts for Transesterification of Soybean Oil with Methanol. *Ind. Eng. Chem. Res.* **2012**, *51*, 225−231.
(21) Xie, W.; Wang, T. Biodiesel Production from Soybean Oil Transesterification Using Tin Oxide-Supported WO3 Catalysts. *Fuel Process. Technol.* **2013**, *109*, 150−155.
(22) Dias, J. M.; Alvim-Ferraz, M. C. M.; Almeida, M. F.; Méndez Díaz, J. D.; Polo, M. S.; Utrilla, J. R. Selection of Heterogeneous Catalysts for Biodiesel Production from Animal Fat. *Fuel* **2012**, *94*, 418−425.
(23) Macedo, C. C. S.; Abreu, F. R.; Tavares, A. P.; Alves, M. B.; Zara, L. F.; Rubim, J. C.; Suarez, P. A. Z. New Heterogeneous Metal-Oxides Based Catalyst for Vegetable Oil Trans-Esterification. *J. Braz. Chem. Soc.* **2006**, *17*, 1291−1296.
(24) Molaei Dehkordi, A.; Ghasemi, M. Transesterification of Waste Cooking Oil to Biodiesel Using Ca and Zr Mixed Oxides as Heterogeneous Base Catalysts. *Fuel Process. Technol.* **2012**, *97*, 45−51.
(25) Olatundun, E. A.; Borokini, O. O.; Betiku, E. Cocoa Pod Husk-Plantain Peel Blend as a Novel Green Heterogeneous Catalyst for Renewable and Sustainable Honne Oil Biodiesel Synthesis: A Case of Biowastes-to-Wealth. *Renewable Energy* **2020**, *166*, 163−175.
(26) Miladinović, M. R.; Zdujić, M. V.; Veljović, D. N.; Krstić, J. B.; Banković-Ilić, I. B.; Veljković, V. B.; Stamenković, O. S. Valorization of Walnut Shell Ash as a Catalyst for Biodiesel Production. *Renewable Energy* **2020**, *147*, 1033−1043.
(27) Chen, G. Y.; Shan, R.; Shi, J. F.; Yan, B. B. Transesterification of Palm Oil to Biodiesel Using Rice Husk Ash-Based Catalysts. *Fuel Process. Technol.* **2015**, *133*, 8−13.
(28) Laskar, I. B.; Gupta, R.; Chatterjee, S.; Vanlalveni, C.; Rokhum, L. Taming Waste: Waste Mangifera Indica Peel as a Sustainable Catalyst for Biodiesel Production at Room Temperature. *Renewable Energy* **2020**, *161*, 207−220.
(29) Basumatary, B.; Basumatary, S.; Das, B.; Nath, B.; Kalita, P. Waste Musa Paradisiaca Plant: An Efficient Heterogeneous Base Catalyst for Fast Production of Biodiesel. *J. Clean. Prod.* **2021**, *305*, 127089.
(30) Ayoola, A. A.; Hymore, F. K.; Omonhinmin, C. A.; Agboola, O.; Alagbe, E. E.; Oyekunle, D.; Bello, M. O. Biodiesel production from used vegetable oil and CaO catalyst impregnated with KNO3 and NaNO3. *AIMS Energy* **2020**, *8*, 527−537.
(31) Ibrahim, Y.; Idris, J.; Muhammed, Z.; Danlami, A. M. Synthesis, Characterization and Formation of KNO3 Treated CaO-MgO Composite Catalysts for Biodiesel Production Using Neem Seed Oil. *J. Mater. Environ. Sci.* **2020**, *11*, 781−787.
(32) Babajide, O.; Petrik, L.; Musyoka, N.; Amigun, B.; Ameer, F.Application of Coal Fly Ash as a Solid Basic Catalyst in Producing Biodiesel. *AIChE Annual Meeting, Conference Proceedings*, 2010.
(33) Peña, R.; Romero, R.; Martínez, S. L.; Natividad, R.; Ramírez, A. Characterization of KNO3/NaX Catalyst for Sunflower Oil Transesterification. *Fuel* **2013**, *110*, 63−69.
(34) Fusade, L.; Viles, H.; Wood, C.; Burns, C. The Effect of Wood Ash on the Properties and Durability of Lime Mortar for Repointing Damp Historic Buildings. *Constr. Build. Mater.* **2019**, *212*, 500−513.
(35) deBarros, S. S.; Pessoa Junior, W. A. G.; Sá, I. S. C.; Takeno, M. L.; Nobre, F. X.; Pinheiro, W.; Manzato, L.; Iglauer, S.; de Freitas, F. A. Pineapple (Ananás comosus) leaves ash as a solid base catalyst for biodiesel synthesis. *Bioresour. Technol.* **2020**, *312*, 123569.
(36) Nath, B.; Kalita, P.; Das, B.; Basumatary, S. Highly Efficient Renewable Heterogeneous Base Catalyst Derived from Waste Sesamum Indicum Plant for Synthesis of Biodiesel. *Renewable Energy* **2020**, *151*, 295−310.
(37) Acchar, W.; Dultra, E. J. V.; Segadães, A. M. Untreated Coffee Husk Ashes Used as Flux in Ceramic Tiles. *Appl. Clay Sci.* **2013**, *75−76*, 141−147.
(38) Naveenkumar, R.; Baskar, G. Biodiesel Production from Calophyllum Inophyllum Oil Using Zinc Doped Calcium Oxide (Plaster of Paris) Nanocatalyst. *Bioresour. Technol.* **2019**, *280*, 493−496.
(39) Sharikh, A. M.; Sulaiman, S.; Azmi, A. S.; Sulaiman, S. Z. Potassium Carbonate from Pineapple and Orange Peels as Catalyst for Biodiesel Production. *AIP Conf. Proc.* **2018**, *2030*, 020290.
(40) Fraile, J. M.; García, N.; Mayoral, J. A.; Pires, E.; Roldán, L. The Basicity of Mixed Oxides and the Influence of Alkaline Metals: The Case of Transesterification Reactions. *Appl. Catal. A Gen* **2010**, *387*, 67−74.
(41) Vyas, A. P.; Subrahmanyam, N.; Patel, P. A. Production of Biodiesel through Transesterification of Jatropha Oil Using KNO3/Al2O3 Solid Catalyst. *Fuel* **2009**, *88*, 625−628.
(42) Quah, R. V.; Tan, Y. H.; Mubarak, N. M.; Kansedo, J.; Khalid, M.; Abdullah, E. C.; Abdullah, M. O. Magnetic Biochar Derived from Waste Palm Kernel Shell for Biodiesel Production via Sulfonation. *Waste Manag.* **2020**, *118*, 626−636.
(43) Rosset, M.; Perez-Lopez, O. W. FTIR Spectroscopy Analysis for Monitoring Biodiesel Production by Heterogeneous Catalyst. *Vib. Spectrosc.* **2019**, *105*, 102990.
(44) Mahamuni, N. N.; Adewuyi, Y. G. Fourier Transform Infrared Spectroscopy (FTIR) Method To Monitor Soy Biodiesel and Soybean Oil in Transesterification Reactions, Petrodiesel−Biodiesel Blends, and Blend Adulteration with Soy Oil. *Energy Fuels* **2009**, *23*, 3773−3782.
(45) De Filippis, P.; Giavarini, C.; Scarsella, M.; Sorrentino, M. Transesterification Processes for Vegetable Oils: A Simple Control Method of Methyl Ester Content. *J. Am. Oil Chem. Soc.* **1995**, *72*, 1399−1404.
(46) Reshad, A. S.; Tiwari, P.; Goud, V. V. Extraction of Oil from Rubber Seeds for Biodiesel Application: Optimization of Parameters. *Fuel* **2015**, *150*, 636−644.
(47) Reshad, A. S.; Panjiara, D.; Tiwari, P.; Goud, V. V. Two-Step Process for Production of Methyl Ester from Rubber Seed Oil Using Barium Hydroxide Octahydrate Catalyst: Process Optimization. *J. Clean. Prod.* **2017**, *142*, 3490−3499.
(48) Sarno, M.; Iuliano, M. Biodiesel Production from Waste Cooking Oil. *Green Process. Synth.* **2019**, *8*, 828−836.
(49) Mandari, V.; Devarai, S. K. Biodiesel Production Using Homogeneous, Heterogeneous, and Enzyme Catalysts via Transesterification and Esterification Reactions: A Critical Review. *Bioenergy Res.* **2022**, *15*, 935−961.
(50) Ullah, Z.; Bustam, M. A.; Man, Z. Characterization of Waste Palm Cooking Oil for Biodiesel Production. *Int. J. Chem. Eng.* **2014**, *5*, 134−137.
(51) Deng, X.; Fang, Z.; Liu, Y. H. Ultrasonic Transesterification of Jatropha Curcas L. Oil to Biodiesel by a Two-Step Process. *Energy Convers. Manag.* **2010**, *51*, 2802−2807.
(52) Cai, J.; He, Y.; Yu, X.; Banks, S. W.; Yang, Y.; Zhang, X.; Yu, Y.; Liu, R.; Bridgwater, A. V. Review of Physicochemical Properties and Analytical Characterization of Lignocellulosic Biomass. *Renew. Sustain. Energy Rev.* **2017**, *76*, 309−322.
(53) Afessa, M. M.; Debiagi, P.; Ferreiro, A. I.; Mendes, M. A. A.; Faravelli, T.; Ramayya, A. V. Experimental and Modeling Investigation on Pyrolysis of Agricultural Biomass Residues: Khat Stem and Coffee Husk for Bio-Oil Application. *J. Anal. Appl. Pyrolysis* **2022**, *162*, 105435.
(54) Haykırı-Açma, H. Combustion Characteristics of Different Biomass Materials. *Energy Convers. Manag.* **2003**, *44*, 155−162.
(55) Kabayo, S. M.; Kindala, J. T.; Nkanga, C. I.; Krause, R. W. M.; Taba, K. M. Preparation and Characterization of Solid Acid Catalysts Derived from Coffee Husks. *Int. J. Chem. Sci.* **2019**, *3*, 5−13.

https://doi.org/10.1021/acsomega.2c05572
ACS Omega 2022, 7, 45129−45143

(56) Kiggundu, N.; Sittamukyoto, J. Pryloysis of Coffee Husks for Biochar Production. *J. Environ. Protect.* **2019**, *10*, 1553.
(57) Amertet, S.; Mitiku, Y.; Belete, G. Analysis of a Coffee Husk Fired Cogeneration Plant in South Western Ethiopia Coffee Processing Industries. *Low Carbon Econ.* **2021**, *12*, 42−62.
(58) Ballesteros, L. F.; Teixeira, J. A.; Mussatto, S. I. Chemical, Functional, and Structural Properties of Spent Coffee Grounds and Coffee Silverskin. *Food Bioprocess Technol.* **2014**, *7*, 3493−3503.
(59) Patil, R. C.; Patil, U. P.; Jagdale, A. A.; Shinde, S. K.; Patil, S. S. Ash of pomegranate peels (APP): A bio-waste heterogeneous catalyst for sustainable synthesis of α,α'-bis(substituted benzylidine)-cycloalkanones and 2-arylidene-1-tetralones. *Res. Chem. Intermed.* **2020**, *46*, 3527−3543.
(60) Garskaite, E.; Gross, K. A.; Yang, S. W.; Yang, T. C. K.; Yang, J. C.; Kareiva, A. Effect of Processing Conditions on the Crystallinity and Structure of Carbonated Calcium Hydroxyapatite (CHAp). *CrystEngComm* **2014**, *16*, 3950−3959.
(61) Kim, W.; Zhang, Q.; Saito, F. Mechanochemical Synthesis of Hydroxyapatite from Ca(OH)2-P2O5 and CaO-Ca(OH)2-P2O5 Mixtures. *J. Mater. Sci.* **2000**, *35*, 5401−5405.
(62) Zinla, D.; Gbaha, P.; Koffi, P. M. E.; Koua, B. K. Characterization of rice, coffee and cocoa crops residues as fuel of thermal power plant in Côte d'Ivoire. *Fuel* **2021**, *283*, 119250.
(63) Song, H.; Fan, H.; Gao, H. T.; Liu, J. A.; Mou, H. Improving Fly Ash Brightness with Carbon and Iron Oxide Removal. *Recycling* **2020**, *5*, 5.
(64) Sharma, M.; Khan, A. A.; Puri, S. K.; Tuli, D. K. Wood Ash as a Potential Heterogeneous Catalyst for Biodiesel Synthesis. *Biomass Bioenergy* **2012**, *41*, 94−106.
(65) Pham Minh, D.; Rio, S.; Sharrock, P.; Sebei, H.; Lyczko, N.; Tran, N. D.; Raii, M.; Nzihou, A. Hydroxyapatite Starting from Calcium Carbonate and Orthophosphoric Acid: Synthesis, Characterization, and Applications. *J. Mater. Sci.* **2014**, *49*, 4261−4269.
(66) Gámiz, B.; Hall, K.; Spokas, K. A.; Cox, L. Understanding Activation Effects on Low-Temperature Biochar for Optimization of Herbicide Sorption. *Agronomy* **2019**, *9*, 588.
(67) Pavankumar, K.; Venkateswarlu, K.; Rameshbabu, N.; Muthupandi, V. X-Ray Peak Broadening and in-Vitro Dissolution Studies of Thermally Stabilized Nanocrystalline Carbonated Hydroxyapatite. *Key Eng. Mater.* **2012**, *493*−*494*, 739−745.
(68) Bano, N.; Jikan, S. S.; Basri, H.; Adzila, S.; Zago, D. M. XRD and FTIR Study of A&B Type Carbonated Hydroxyapatite Extracted from Bovine Bone. *AIP Conf. Proc.* **2019**, *2068*, 20100.
(69) Sulaiman, N. F.; Hashim, A. N. N.; Toemen, S.; Rosid, S. J. M.; Mokhtar, W. N. A. W.; Nadarajan, R.; Bakar, W. A. W. A. Biodiesel Production from Refined Used Cooking Oil Using Co-Metal Oxide Catalyzed Transesterification. *Renewable Energy* **2020**, *153*, 1−11.
(70) Basumatary, B.; Das, B.; Nath, B.; Basumatary, S. Synthesis and Characterization of Heterogeneous Catalyst from Sugarcane Bagasse: Production of Jatropha Seed Oil Methyl Esters. *Curr. Res. Green Sustain. Chem.* **2021**, *4*, 100082.
(71) Veiga, T. R. L. A.; Lima, J. T.; Dessimoni, A. L. de A.; Pego, M. F. F.; Soares, J. R.; Trugilho, P. F. Different Plant Biomass Characterizations for Biochar Production. *Cerne* **2017**, *23*, 529−536.
(72) Wang, H.; Xiao, Z.; Yang, J.; Lu, D.; Kishen, A.; Li, Y.; Chen, Z.; Que, K.; Zhang, Q.; Deng, X.; Yang, X.; Cai, Q.; Chen, N.; Cong, C.; Guan, B.; Li, T.; Zhang, X. Oriented and Ordered Biomimetic Remineralization of the Surface of Demineralized Dental Enamel Using HAP@ACP Nanoparticles Guided by Glycine. *Sci. Rep.* **2017**, *7*, 40701.
(73) Udhayakumar, G.; Muthukumarasamy, N.; Velauthapillai, D.; Santhosh, S. B. Correction to: Highly Crystalline Zinc Incorporated Hydroxyapatite Nanorods' Synthesis, Characterization, Thermal, Biocompatibility, and Antibacterial Study. *Appl. Phys. A* **2017**, *123*, 655.
(74) Olaru, M.; Aflori, M.; Simionescu, B.; Doroftei, F.; Stratulat, L. Effect of SO2 Dry Deposition on Porous Dolomitic Limestones. *Materials* **2010**, *3*, 216−231.
(75) Landi, E.; Celotti, G.; Logroscino, G.; Tampieri, A. Carbonated Hydroxyapatite as Bone Substitute. *J. Eur. Ceram. Soc.* **2003**, *23*, 2931−2937.
(76) Kim, J. H.; Lee, G.; Park, J. E.; Kim, S. H. Limitation of K2co3 as a Chemical Agent for Upgrading Activated Carbon. *Processes* **2021**, *9*, 1000.
(77) Permatasari, H. A.; Yusuf, Y. Characteristics of Carbonated Hydroxyapatite Based on Abalone Mussel Shells (Halioitis Asinina) Synthesized by Precipitation Method with Aging Time Variations. *IOP Conf. Ser.: Mater. Sci. Eng.* **2019**, *546*, 042031.
(78) Talebian-Kiakalaieh, A.; Amin, N. A. S.; Mazaheri, H. A Review on Novel Processes of Biodiesel Production from Waste Cooking Oil. *Appl. Energy* **2013**, *104*, 683−710.
(79) Sharma, Y. C.; Singh, B.; Madhu, D.; Liu, Y.; Yaakob, Z. Fast Synthesis of High Quality Biodiesel from "waste Fish Oil" by Single Step Transesterification. *Biofuel Res. J.* **2014**, *1*, 78−80.

https://doi.org/10.1021/acsomega.2c05572
ACS Omega 2022, 7, 45129−45143